Spherical-deformed shape coexistence for the *pf* shell in the nuclear shell model

Takahiro Mizusaki,[1] Takaharu Otsuka,[2,3] Michio Honma,[4] and B. Alex Brown[5]
[1]*Department of Law, Senshu University, Higashimita, Tama, Kawasaki, Kanagawa 214-8580, Japan*
[2]*Department of Physics, University of Tokyo, Hongo, Tokyo 113-0033, Japan*
[3]*RIKEN, Hirosawa, Wako-shi, Saitama 351-0198, Japan*
[4]*Center for Mathematical Sciences, University of Aizu, Tsuruga, Ikki-machi Aizu-Wakamatsu, Fukushima 965-8580, Japan*
[5]*National Superconducting Cyclotron Laboratory and Department of Physics and Astronomy, Michigan State University, East Lansing, Michigan 48824-1321*
(Received 19 October 2000; published 5 March 2001)

A spherical-deformed shape coexistence for semimagic *pf*-shell nuclei is investigated. Deformed states can arise by breaking the $f_{7/2}$ submagic shell, and coexist with spherical yrast states for ^{54}Fe. These states are shown to be primarily two-particle two-hole excitations on top of the respective correlated ground states. In addition to these modes, a four-particle–four-hole excitation can be found for ^{54}Fe, which is related to the deformed band of doubly magic ^{56}Ni. To investigate this shape coexistence, we use the conventional shell-model diagonalization, constrained Hartree-Fock, generator coordinate, variation-after-projection, and Monte Carlo shell-model methods.

DOI: 10.1103/PhysRevC.63.044306 PACS number(s): 24.10.Cn, 21.60.Cs, 21.10.Re, 27.40.+z

I. INTRODUCTION

Coexistence between spherical and deformed shapes can take place rather predominantly in and near semimagic or doubly magic nuclei. A clear example of such shape coexistence occurs in the Sn isotopes, where the yrast states are spherical, while deformed intruder bands appear at low excitation energy for $^{110-120}$Sn (for a review, see Ref. [1]). In general, a closed magic shell leads to a spherical configuration for yrast states, while the coexisting deformed mode is produced by breaking the magic shell. The stability of the spherical equilibrium helps to assure the presence of a deformed minimum due to its orthogonal structure.

Recently, such a spherical-deformed shape coexistence has been experimentally found in the doubly magic nucleus ^{56}Ni [2]. For the description of this spherical-deformed shape coexistence, shell-model and mean-field approaches [2,3] are both suitable. The shell-model approach has the advantage that it can handle spherical and deformed states on the same footing within a single theoretical framework. Therefore ^{56}Ni has been a frontier for state-of-the-art large-scale shell-model diagonalizations [2,3] and new methods of shell-model calculations [3–10]. In Ref. [3], by using the constrained Hartree-Fock, generator coordinate, and Monte Carlo shell-model methods, we successfully described this shape coexistence within the *pf*-shell model space using the FPD6 realistic residual shell-model interaction [11]. In this paper we investigate the spherical-deformed shape coexistence in a wider range of *pf*-shell nuclei with $N=28$ which includes the doubly magic nuclei ^{48}Ca and ^{56}Ni and the semimagic nuclei ^{50}Ti, ^{52}Cr, and ^{54}Fe. This investigation provides a deeper understanding of the deformed band of ^{56}Ni. To solve the shell model problem, the conventional shell-model diagonalization, the potential energy surface (PES) generated from the constrained Hartree-Fock (CHF) method, the generator coordinate method (GCM), variation-after-projection (VAP), and the Monte-Carlo shell-model (MCSM) approach are taken.

This paper is organized as follows. In the next section we discuss the shell-model calculation by the various methods mentioned above: CHF, large-scale shell-model diagonalizations, GCM, VAP, and Monte Carlo. The third section is devoted to a discussion of the spherical-deformed shape coexistence in the $N=28$ magic nuclei. In the last section, we present a summary. All calculations are based upon the *pf* shell-model space with the FPD6 realistic residual interaction [11]. The quadrupole matrix elements are calculated with the same values of the effective charges $e_p=1.23e$ and $e_n=0.54e$, as used in Refs. [3,7].

II. SHELL-MODEL METHODS

A. Constrained Hartree-Fock

In the CHF [12] one constructs a PES, which is used to visualize the mean-field structure embedded in the shell-model space in terms of the quadrupole degrees of freedom as shown in Ref. [3]. Here we take q (the intrinsic quadrupole moment) and γ (the triaxial angle) as constrained parameters. In Fig. 1, contour plots for the PES's are shown for the $N=28$ nuclei ^{52}Cr-^{56}Ni. The PES's for ^{52}Cr, ^{54}Fe, and ^{56}Ni show two minima, suggesting a spherical-deformed

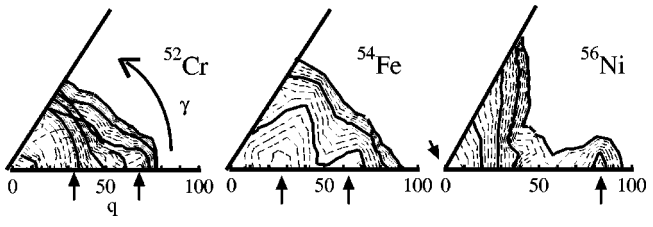

FIG. 1. PES's on the q-γ plane for ^{52}Cr-^{56}Ni. The dotted contours are separated by 0.3 MeV. The solid contours are separated by 1.5 MeV. The local minima are indicated by arrows.

TABLE I. Occupation numbers for $f_{7/2}$, $p_{3/2}$, $f_{5/2}$, and $p_{1/2}$ orbits for the CHF states at the spherical and deformed local minima. The second column is the value of q at the local minimum. Columns 3–6 correspond to the occupation numbers for neutron/proton orbits.

Nucleus	q (fm^2)	$f_{7/2}$	$p_{3/2}$	$f_{5/2}$	$p_{1/2}$
^{52}Cr	35	7.6/3.7	0.3/0.2	0.1/0.1	0.0/0.0
	70	5.4/3.1	0.8/0.7	1.3/0.2	0.5/0.0
^{54}Fe	30	7.7/5.7	0.2/0.2	0.1/0.1	0.0/0.0
	65	5.6/5.4	0.7/0.4	1.2/0.2	0.5/0.0
^{56}Ni	0	8.0/8.0	0.0/0.0	0.0/0.0	0.0/0.0
	85	5.4/5.4	0.8/0.8	1.4/1.4	0.4/0.4

shape coexistence. One is spherical and the other is prolate. Prolate minima are located at $q=70$, 65, and 85 $e$fm^2, and $\gamma=0$ for ^{52}Cr, ^{54}Fe, and ^{56}Ni, respectively. For ^{52}Cr and ^{54}Fe, the PES's are rather shallow, while for ^{56}Ni, the PES forms a pronounced prolate minimum with an axial ($\gamma=0$) nature.

Next we consider the configuration of these prolate minima. The configurations of the CHF states at the local minima are shown in Table I. For ^{54}Fe, the occupation numbers of upper orbits ($f_{5/2}$, $p_{3/2}$, and $p_{1/2}$) are 0.6 and 3.0 for spherical and prolate minima, respectively. Although ^{54}Fe is a semimagic nucleus, the ground state corresponding to this spherical minimum, is composed of various components in addition to $(f_{7/2})^{14}$ configuration. Therefore we call it the correlated ground state hereafter. By subtracting these two occupation numbers, on average, 2.4 nucleons (2.1 neutrons and 0.3 protons) are excited (relative to the correlated ground state) from the $f_{7/2}$ orbit into the upper orbits. Thus, in terms of the occupation numbers, these states are related to the correlated ground state by the excitation of approximately two neutrons out of the $f_{7/2}$ shell. We will refer to these states as ''correlated two-particle–two-hole ($2p$-$2h$)'' states where $f_{5/2}$, $p_{3/2}$, and $p_{1/2}$ are the particle states and $f_{7/2}$ is the hole state. The ''correlated $4p$-$4h$'' states will be those in which approximately four $f_{7/2}$ particles are excited out of the correlated ground state. The orbit occupations of these neutron excitations are similar to those of the neutron component of the deformed (correlated $4p$-$4h$) state of ^{56}Ni. Thus at the mean-field level, spherical-deformed shape coexistence is suggested for ^{52}Cr, ^{54}Fe, and ^{56}Ni. Core excited configurations (e.g., coexistence) were first discussed for ^{54}Fe in Ref. [15]. Heyde *et al.* also suggested [1] the shape coexistence for ^{54}Fe and its neighboring even-odd nuclei.

B. Large-scale shell-model diagonalization

Large-scale shell-model calculations are often carried out in the *M* scheme, where a Hamiltonian matrix, constructed from basis with a fixed total magnetic quantum number, is diagonalized. Recent largest shell model calculations have been carried out by Ur *et al.* [16]. Their largest shell model dimension reached about 10^8. We have also developed a new *M*-scheme shell model code MSHELL [17], which could handle a shell-model problem with dimensions up to 1×10^8 on a current workstation or parallel computer.

The *M*-scheme dimensions for ^{48}Ca–^{56}Ni are 10^4–10^9. As the mass number increases, the shell-model dimension rapidly increases. The dimensions for ^{48}Ca, ^{50}Ti, and ^{52}Cr are within the limit of our shell model code, while for ^{54}Fe and ^{56}Ni, a diagonalization with a full shell-model space is not yet available. However, shell-model diagonalization with a truncated shell-model space is still feasible. We use the truncation scheme $\oplus_{s\leq t}(f_{7/2})^{A-40-s}(r)^s$ where r means the set of the $f_{5/2}$, $p_{3/2}$, and $p_{1/2}$ orbits and t is the maximum number of particles allowed to be excited. This truncation scheme is natural because there is some gap between $f_{7/2}$ orbit and the others. For ^{54}Fe, up to a $t=7$ calculation is feasible by our code. By such truncated shell model calculations, we could get well-converged energy eigenvalues for yrast states. However, for nonyrast states which have a correlated $2p$-$2h$ or $4p$-$4h$ structure, we need several eigenstates with the same angular momentum. This requires a larger number of iterations in the Lanczos process, and the diagonalization is much more time consuming and storage requirement becomes extremely severe compared to the yrast states. Currently such a shell model calculation for ^{54}Fe and ^{56}Ni is still quite difficult.

C. GCM calculations

A description more realistic than the CHF picture can be achieved by carrying out a GCM calculation within the *pf* shell-model space [3,12–14]. The GCM uses various CHF states specified by collective coordinates. Here we have carried out GCM calculations with $\vec{q}=(q,\gamma)$. The GCM wave function is written as

$$|\Psi_{JM}\rangle=\int d\vec{q} f_{JM}(\vec{q})|\Phi_{JM}(\vec{q})\rangle \tag{1}$$

by superposing the projected CHF state $|\Phi_{JM}(\vec{q})\rangle$, where $f_{JM}(\vec{q})$ are the amplitudes of each projected wave function $|\Phi_{JM}(\vec{q})\rangle$. Here the projected wave function is determined by

$$|\Phi_{JM}(\vec{q})\rangle=\sum_{K=-J}^{J} g_K P^J_{M,K}|\phi(\vec{q})\rangle, \tag{2}$$

where $|\phi(\vec{q})\rangle$ is a CHF states at $\vec{q}$ and the g_K is determined by the diagonalization for each basis. To determine the amplitude $f_{JM}(\vec{q})$, we evaluate the Hamiltonian and norm projected matrix elements as

$$\begin{Bmatrix} H^J_{KK'}(\vec{q},\vec{q}') \\ N^J_{KK'}(\vec{q},\vec{q}') \end{Bmatrix} = \left\langle \phi(\vec{q}') \middle| \begin{Bmatrix} H \\ 1 \end{Bmatrix} P^J_{KK'} \middle| \phi(\vec{q}) \right\rangle \tag{3}$$

and we solve the generalized eigenvalue problem.

As an example, we take ^{54}Fe. We represent the (q,γ) plane by 121 mesh points. Then we solve the generalized eigenvalue problem. In Fig. 2, we show the results of the triaxial GCM. For each spin, we show the lowest 13 states.

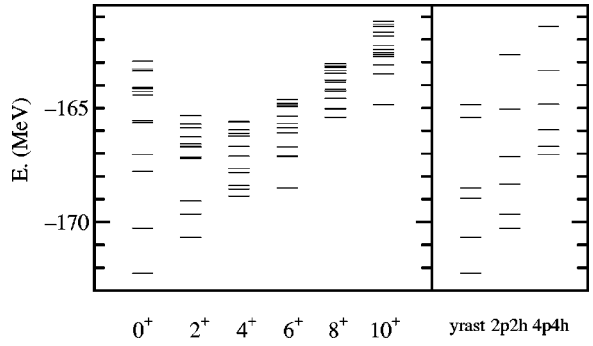

FIG. 2. GCM eigenenergies for ^{54}Fe in triaxial GCM. Among three levels, yrast, correlated $2p$-$2h$ and correlated $4p$-$4h$ states are selected shown for $J=0$, 2, 4, 6, 8, and 10 in the right-hand part.

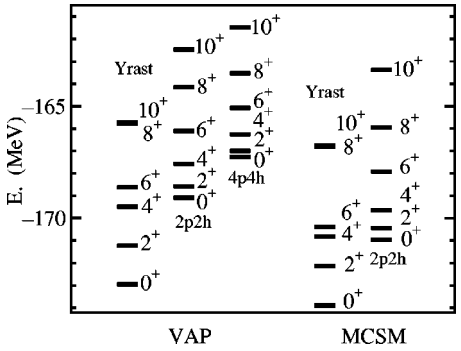

FIG. 3. VAP and MCSM level schemes for ^{54}Fe

The spherical yrast and correlated $2p$-$2h$ (deformed) states are fragmented, but the levels characterized predominantly by this nature are shown as the bands on the right-hand side of Fig. 2. In the triaxial calculation, the ground state is lowered by 5.2 MeV compared to the HF energy. The total correlation is defined by the difference between the HF and exact energies. As this energy is about 6.5 MeV, the GCM calculation is good as an approximation. This is due to the mixing among the GCM bases and angular momentum projection.

Furthermore, it is interesting that a correlated $4p$-$4h$ band appears, which is shown on the right-hand side of Fig. 2. This mode was not anticipated in the PES. The correlated $4p$-$4h$ character of this band is determined by analyzing the occupation numbers. The deformation of this correlated $4p$-$4h$ band is significantly larger than that of the correlated $2p$-$2h$ band and is similar to the correlated $4p$-$4h$ band of ^{56}Ni [3]. The nature of this correlated $4p$-$4h$ mode will be further discussed in the next subsection.

D. Variation after projection

To go beyond a mean-field description, the VAP and GCM methods are known to be useful. In the VAP method, we consider the angular momentum projected energy surface (J-energy surface) of a given shell-model Hamiltonian, which is general and is not restricted by the collective coordinates. In the VAP, we consider the variation

$$\delta\left[\frac{\langle\Psi_{JM}|H|\Psi_{JM}\rangle}{\langle\Psi_{JM}|\Psi_{JM}\rangle}\right]=0, \tag{4}$$

where the variational wave function has the same form as Eq. (2), except the variational parameters $\vec{q}$. Here the variational parameters are g_K and $|\phi\rangle$ itself. We solve this variational problem by the gradient method [18]. As there are several energy minima in the J-energy surface, we can obtain several solutions in the VAP method. In the VAP, the number of variational parameters is too large to graphically visualize the energy surface. Therefore, we mathematically judge local minimum when the norm of gradient vector vanishes.

The VAP results for ^{54}Fe are shown in Fig. 3. For the ^{54}Fe ground state, the VAP calculation gives a lower energy than GCM calculation. The improvement is due to the correlation out of the q-γ plane, while the VAP energy is still about 1 MeV higher than the $t=7$ shell-model diagonalization. For the yrast level scheme, the VAP level scheme is similar to those of $t=7$ diagonalization.

In the VAP we also find a local minimum in the J-energy surface for the correlated $2p$-$2h$ mode as expected from the PES and GCM. These local minima are not very well defined in J-energy surface because the norm of gradient vector becomes small but is not zero. In Fig. 3, the energy spectrum for the correlated $2p$-$2h$ mode is shown at the point when the norm of gradient vector is smallest. This energy is higher than that of GCM. The correlated $2p$-$2h$ states are strongly coupled with states nearby. The quadrupole moments are -30, -39, -39, -39, and -38 for the 2^+, 4^+, 6^+, 8^+, and 10^+ states, respectively.

The correlated $4p$-$4h$ mode is quite interesting because this mode has no minimum in the PES, while in the J-energy surface, these states form a distinct local minima. The quadrupole moments are -42, -55, -56, -59, and -61 for 2^+, 4^+, 6^+, 8^+, and 10^+, respectively. The $f_{7/2}$ occupation number is rather constant concerning spin with values of 3.3 to 3.4 for protons and 5.2 to 5.3 for neutrons. The excited nucleon number is about 2.7 for both protons and neutrons which is quite similar to the deformed band of ^{56}Ni [3].

Here we note that, in stead of HF, the VAP based upon the Hartree-Fock-Bogoliubov method is considered to give a better approximation. Such a method and its extension have been developed by the Tübingen group [10,20].

E. Monte Carlo shell model

In order to obtain a more accurate description, we move to the Monte Carlo shell model. Within one projected Slater determinant, VAP is the best method. To improve the VAP approximation, we should express eigenstates by projected multi-Slater determinants. The GCM calculation meets this requirement but its multi-Slater determinants are restricted by generator coordinates. Namely, the GCM is a diagonalization of the shell-model Hamiltonian within the truncated shell-model space concerning the quadrupole degrees of freedom. To evaluate shell-model eigenstates precisely, we should express eigenstates by well-optimized projected multi-Slater determinants without any shape assumption. The

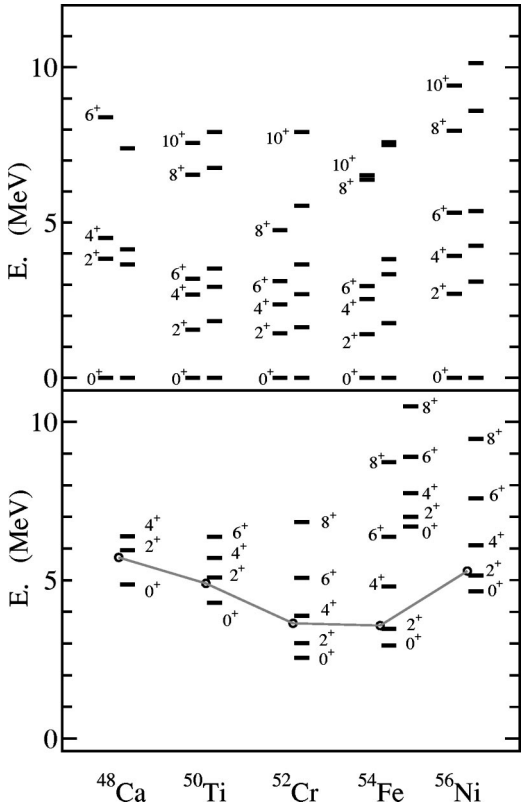

FIG. 4. Level schemes for ^{48}Ca-^{56}Ni. In the upper panel, spherical yrast states are shown, while in the lower panel, nonyrast states are summarized. Two columns are paired for each nucleus. In the upper panel, the left level scheme is experimental data and the right one is the results of the shell-model diagonalization calculations. In the lower panel, the results of shell-model calculations for the correlated $2p$-$2h$ and $4p$-$4h$ states are shown. The open circles (connected by gray lines to guide the eye) are the results of the weak-coupling scheme. Experimental data are taken from Refs. [2,21].

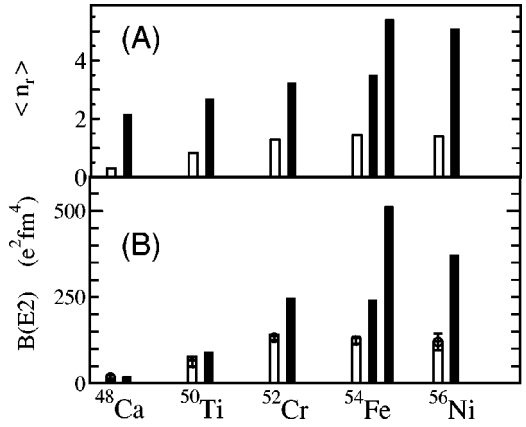

FIG. 5. (a) The average number of nucleons excited from the $f_{7/2}$ orbit (n_r) for the 0_1^+ (white bar) and 0_p^+ (black bar) states in ^{48}Ca-^{56}Ni. For ^{54}Fe, the results of correlated $4p$-$4h$ mode are added. (b) $B(E2{:}2^+ \rightarrow 0^+)$ values are shown. Open circles are the experimental data [22,23].

problem is how to choose the set of Slater determinants. This problem is solved within the QMCD method as discussed in Refs. [4–7].

The results for yrast and correlated $2p$-$2h$ (prolate) states in ^{54}Fe are shown in Fig. 3. For the calculation of the nonyrast states, we must take into account the orthogonality among eigenstates. As shown in Fig. 3, the eigenenergies of the MCSM results are several MeV lower than the VAP. At present the correlated $4p$-$4h$ deformed mode is too high in excitation energy and appears to be outside the practically applicable region of the MCSM calculation.

III. SHAPE COEXISTENCE IN THE $N=28$ NUCLEI

A. Systematics of $N=28$ magic nuclei

Now we focus on the systematics of the spherical-deformed shape coexistence for the entire set of even-even *pf*-shell nuclei with $N=28$. We start with the doubly magic nuclei ^{48}Ca and ^{56}Ni. The ^{48}Ca nucleus has no valence protons (in the *pf* shell). The PES of ^{48}Ca is completely spherical. The ground state is composed mainly (90%) of the $(f_{7/2})^8$ configuration, which indicates that ^{48}Ca is a good doubly magic nucleus. The low-lying states are neutron $2p$-$2h$ states and are the neutron pairing vibration modes [19]. On the other hand, the ^{56}Ni nucleus has eight protons and eight neutrons in the *pf* shell. The partial shell-gap between the $f_{7/2}$ and the other *pf*-shell orbits gives rise to an interesting feature. Contrast with ^{48}Ca, ^{56}Ni has a rather soft spherical yrast band with a well developed excited deformed band. This deformed band has been recently observed experimentally [2]. The PES analysis in Fig. 1 indicates this deformed band. The MCSM calculation with the FPD6 interaction can describe this spherical-deformed shape coexistence quite well [3,7] and it clarifies that this deformed band represents a four-particle–four-hole excitation on top of the correlated ground state [3]. Thus the doubly magic ^{48}Ca and ^{56}Ni are completely different in structure.

Next we examine how this difference evolves in the structure of the $N=28$ semimagic nuclei in terms of energy levels, $B(E2)$ values, and occupation numbers. In the upper panel of Fig. 4, the spherical yrast states are shown. The ^{48}Ca nucleus is doubly magic and it has a rather large excitation energy for the 2^+ state. The yrast level scheme of ^{50}Ti and ^{54}Fe are composed mainly of the $(f_{7/2})_\pi^2$ or $(f_{7/2})_\pi^{-2}$ configuration with the neutron $f_{7/2}$ closed shell up to 6^+, respectively. These spectra are typical of a $T=1$ short range attractive force. On the other hand, for higher spins, neutrons in the $f_{7/2}$ orbit must be promoted into the upper orbits. Consequently there is a large gap between 6^+ and 8^+. Experimental data and shell-model results clearly show such gaps in both spectra, in a consistent manner. Thus, particle-hole symmetry is seen. On the other hand, the main components of the low spin states of ^{52}Cr should be $(f_{7/2})_\pi^4$ up to 8^+ and the gap should be between the 8^+ and 10^+. The shell-model results show such a tendency, but the wave functions in ^{52}Cr have appreciable mixing with other configurations. Consequently the actual gap is not as pronounced as in ^{50}Ti and ^{54}Fe. Thus, the spherical yrast states are nicely described by the FPD6 interaction.

Next we move to the lower panel of Fig. 4, where the nonyrast states are shown. We will refer to the states of

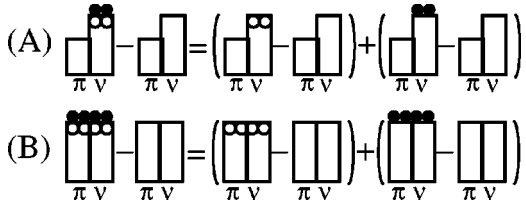

FIG. 6. Schematic explanation of the weak-coupling scheme.

lower panel by subscript p. In Fig. 5 we show expectation value of nucleons excited into the upper orbits (n_r) and the $B(E2)$ values for the ground and 0_p^+ states.

^{50}Ti has a similar $2p$-$2h$ structure as ^{48}Ca, though its 0_p^+ energy is lower. A correlated $2p$-$2h$ 2_p^+ state develops, but the $B(E2)$ and n_r values are not very large. Thus ^{50}Ti shows a transient aspect. For ^{52}Cr and ^{54}Fe, the increase in the number of valence protons lowers the deformed bandhead energy due to the proton-neuron interaction. The n_r for the spherical states increases in ^{52}Cr, and then stays constant for ^{54}Fe and ^{56}Ni. On the other hand, n_r for the 0_p^+ states for ^{48}Ca-^{54}Fe increases roughly in the same way as for the ground states, such that the difference is roughly two. Thus for all of these nuclei the 0_p^+ states are $2p$-$2h$ excitations, built on the correlated ground states (correlated $2p$-$2h$ states). For ^{54}Fe, the correlated $4p$-$4h$ state appears, which has a quite similar n_r as in ^{56}Ni. According to the FPD6 interaction, such a deformed band seems to be a generic feature around ^{56}Ni. The $B(E2)$ values shown in Fig. 5 also indicate the growth of collectivity. The $B(E2)$'s of the yrast states are rather constant and relatively small, while the $B(E2)$'s in the coexisting $2p2h$ mode becomes much larger as the valence proton number increases. The $B(E2)$ of the $4p4h$ mode of ^{54}Fe is much larger than those of $2p2h$ modes in $N=28$ isotones and is similar to the one of the $4p4h$ mode in ^{56}Ni. Thus, the nonyrast modes of $N=28$ isotones can be understood by a correlated $2p$-$2h$ or $4p$-$4h$ excitation mechanism.

B. Weak-coupling scheme

To understand the behavior of the excited bandhead energy, we consider the weak-coupling scheme [25] based on correlated np-mh modes for proton and/or neutron degree of freedom. We start by assuming an effective closed-shell configuration for $N=28$. Then if the average particle-hole interaction is weak (we assume zero here), the excitation energy can be estimated from the experimental binding energies [24] of neighboring nuclei. The bandhead energies of the excited 0^+ of ^{48}Ca are estimated from the binding energies of ^{46,48,50}Ca because ^{50}Ca has two particles on top of the magic core, and ^{46}Ca has two holes. This weak-coupling situation is illustrated in Fig. 6(a). The same picture can be used to estimate the excitation energies of the correlated $2p$-$2h$ neutron excitations for the other semimagic nuclei up to ^{54}Fe. For ^{56}Ni we must consider the excitation of four nucleons (two protons and two neutrons) across $N=28$. The relevant weak coupling picture is depicted in Fig. 6(b). These estimated values are shown in the lower panel of Fig. 6. These weak-coupling estimates, as shown in the bottom of Fig. 4, give the trend and a qualitative value for the excitation energies of these coexisting configurations.

The model of Fig. 6(b) can be extended to give the weak-coupling energies E_w of np-mh states relative to ^{56}Ni in terms of the experimental binding energies of the mp and nh ground states. For example, the excitation energy of the correlated $2p$-$2h$ state in ^{54}Fe is given by $E_w(2p-4h) - E_w(2h) = 1.60$ MeV and the excitation energy of the correlated $4p$-$4h$ state in ^{54}Fe is given by $E_w(4p-6h) - E_w(2h) = 5.71$ MeV. These are again in qualitative agreement with the results discussed in Sec. II. The weak-coupling estimate for the excitation energy of the $8p$-$8h$ configuration in ^{56}Ni is 10.56 MeV. Based upon the fact that there are no minima found in the CHF approach which correspond to this configuration, it would not form a distinct collective band and the states would be mixed with other configurations.

Although these weak-coupling models start out by assuming an $f_{7/2}$ closed-shell at $N=28$, we realize from the discussion in Sec. II, that they actually apply to the ''effective'' or ''correlated'' closed-shell configuration. The correlated closed-shell configuration already contains a considerable amount of excitation energy across the $N=28$ shell gap, and the deformed coexisting states correspond to an additional two or four nucleons excited across the gap. In this sense, the weak-coupling model is dealing with what we call the ''correlated np-nh'' configurations.

IV. CONCLUSION

In summary, in the first part of this paper, we discussed the GCM, VAP, and MCSM approaches for nuclear shell model. In the next part, we reported a shell-model treatment of the spherical-deformed shape coexistence for doubly and semimagic *pf*-shell nuclei. Consistent with a naive shell-model picture, the yrast states are rather spherical and the $f_{7/2}$ configuration dominate the low spin states. As spin goes up, excitations into upper orbits become important and gaps appear in the yrast level scheme of ^{50}Ti, ^{52}Cr, and ^{54}Fe.

A collective deformed mode coexists with the above spherical states. This mode can be understood in terms of the two doubly magic nuclei ^{48}Ca and ^{56}Ni. In the former, a two-neutron pairing vibration mode appears, while in the latter, there exists a clear correlated $4p$-$4h$ deformed band. For semimagic nuclei, a correlated $2p$-$2h$ deformed band rapidly develops as the valence proton number increases. In ^{54}Fe a correlated $4p$-$4h$ mode seems to come down at $E \sim 6$ MeV. The description of this mode needs the consideration of a J-projected energy surface. This mode is quite similar to the correlated $4p$-$4h$ deformed band of ^{56}Ni.

In addition to the shell-model results, we presented a simple argument based on the weak-coupling scheme to understand these states. These estimates rely on experimental binding energies and are free of the shell-model residual interaction. These estimates reinforce our interpretation of deformed bands. Also, our microscopic calculations provide an interpretation of the weak-coupling model in terms of excitations out of a correlated ground state.

ACKNOWLEDGMENTS

We thank Professor S. Pittel for delightful comments. This work was supported in part by Grant-in-Aid for Scientific Research Nos. (A)(2)(10304019) and (B)(2)(10044059) from the Ministry of Education, Science and Culture. B. A. Brown was also supported in part by U.S. NSF Grant No. PHY-0070911. Numerical calculations were carried out by the massively parallel computer Alphleet in RIKEN.

[1] K. Heyde, P. Van Isacker, M. Waroquier, J.L. Wood, and R.A. Meyer, Phys. Rep. **102**, 291 (1983).
[2] D. Rudolf *et al.*, Phys. Rev. Lett. **82**, 3763 (1999).
[3] T. Mizusaki, T. Otsuka, Y. Utsuno, M. Honma, and T. Sebe, Phys. Rev. C **59**, R1846 (1999).
[4] M. Honma, T. Mizusaki, and T. Otsuka, Phys. Rev. Lett. **75**, 1284 (1995).
[5] T. Mizusaki, M. Honma, and T. Otsuka, Phys. Rev. C **53**, 2786 (1996).
[6] M. Honma, T. Mizusaki, and T. Otsuka, Phys. Rev. Lett. **77**, 3315 (1996).
[7] T. Otsuka, M. Honma, and T. Mizusaki, Phys. Rev. Lett. **81**, 1588 (1998).
[8] T. Otsuka, T. Mizusaki, and M. Honma, J. Phys. G **25**, 699 (1999).
[9] S.E. Koonin, D.J. Dean, and K. Langanke, Phys. Rep. **577**, 1 (1996).
[10] A. Petrovici, in *Proceedings of the Conference on SM2000* [Nucl. Phys. (to be published)].
[11] W.A. Richter, M.G. van der Merwe, R.E. Julies, and B.A. Brown, Nucl. Phys. **A523**, 325 (1991); **A577**, 585 (1994).
[12] For instance, P.-H. Heenen, P. Bonche, J. Dobaczewski, and H. Flocard, Nucl. Phys. **A561**, 367 (1993); P. Bonche, J. Dobaczewski, H. Flocard, and P.-H. Heenen, **A530**, 149 (1991).
[13] K. Hara, Y. Sun, and T. Mizusaki, Phys. Rev. Lett. **83**, 1922 (1999).
[14] P. Ring and P. Schuck, *The Nuclear Many-Body Problem* (Springer-Verlag, New York, 1980).
[15] S. Pittel, Phys. Lett. **33B**, 158 (1970).
[16] C.A. Ur *et al.*, Phys. Rev. C **58**, 3163 (1998).
[17] T. Mizusaki, RIKEN Accel. Prog. Rep. **33**, 14 (2000).
[18] J.L. Egido and P. Ring, Nucl. Phys. **A383**, 182 (1982).
[19] B.A. Brown and W.A. Richter, Phys. Rev. C **58**, 2099 (1998).
[20] A. Petrovici, K. W. Schmid, and Amand Faessler, Nucl. Phys. **A665**, 33 (2000), and references therein.
[21] *Table of Isotopes*, edited by R. B. Firestone *et al.* (Wiley, New York, 1996).
[22] S. Raman, At. Data Nucl. Data Tables **36**, 1 (1987).
[23] G. Kraus *et al.*, Phys. Rev. Lett. **73**, 1773 (1994).
[24] G. Audi and A.H. Wapstra, Nucl. Phys. **A565**, 1 (1993).
[25] G. E. Arenas Peris and P. Federman, Phys. Lett. B **173**, 359 (1986).